NASA/CR—2007-215050

Hydrodynamic Force on a Cylinder Oscillating at Low Frequency

Robert F. Berg
National Institute of Standards and Technology, Gaithersburg, Maryland

Minwu Yao and Charles H. Panzarella
Ohio Aerospace Institute, Brookpark, Ohio

December 2007

NASA STI Program . . . in Profile

Since its founding, NASA has been dedicated to the advancement of aeronautics and space science. The NASA Scientific and Technical Information (STI) program plays a key part in helping NASA maintain this important role.

The NASA STI Program operates under the auspices of the Agency Chief Information Officer. It collects, organizes, provides for archiving, and disseminates NASA's STI. The NASA STI program provides access to the NASA Aeronautics and Space Database and its public interface, the NASA Technical Reports Server, thus providing one of the largest collections of aeronautical and space science STI in the world. Results are published in both non-NASA channels and by NASA in the NASA STI Report Series, which includes the following report types:

- TECHNICAL PUBLICATION. Reports of completed research or a major significant phase of research that present the results of NASA programs and include extensive data or theoretical analysis. Includes compilations of significant scientific and technical data and information deemed to be of continuing reference value. NASA counterpart of peer-reviewed formal professional papers but has less stringent limitations on manuscript length and extent of graphic presentations.

- TECHNICAL MEMORANDUM. Scientific and technical findings that are preliminary or of specialized interest, e.g., quick release reports, working papers, and bibliographies that contain minimal annotation. Does not contain extensive analysis.

- CONTRACTOR REPORT. Scientific and technical findings by NASA-sponsored contractors and grantees.

- CONFERENCE PUBLICATION. Collected papers from scientific and technical conferences, symposia, seminars, or other meetings sponsored or cosponsored by NASA.

- SPECIAL PUBLICATION. Scientific, technical, or historical information from NASA programs, projects, and missions, often concerned with subjects having substantial public interest.

- TECHNICAL TRANSLATION. English-language translations of foreign scientific and technical material pertinent to NASA's mission.

Specialized services also include creating custom thesauri, building customized databases, organizing and publishing research results.

For more information about the NASA STI program, see the following:

- Access the NASA STI program home page at *http://www.sti.nasa.gov*

- E-mail your question via the Internet to *help@sti.nasa.gov*

- Fax your question to the NASA STI Help Desk at 301–621–0134

- Telephone the NASA STI Help Desk at 301–621–0390

- Write to:
  NASA Center for AeroSpace Information (CASI)
  7115 Standard Drive
  Hanover, MD 21076–1320

NASA/CR—2007-215050

Hydrodynamic Force on a Cylinder Oscillating at Low Frequency

Robert F. Berg
National Institute of Standards and Technology, Gaithersburg, Maryland

Minwu Yao and Charles H. Panzarella
Ohio Aerospace Institute, Brookpark, Ohio

Prepared under Contract C–32067–J

National Aeronautics and
Space Administration

Glenn Research Center
Cleveland, Ohio 44135

December 2007

Acknowledgments

We thank Mike Moldover for many helpful discussions and for inspiring the creation of CVX-2. The CVX-2 flight instrument was developed by the engineering team led by Jim Myers at Zin-Tech, Inc. We thank especially Don Priebe, the chief electrical engineer, who ran the flight instrument to obtain the experimental data. We thank Professor Bearman for permission to adapt Figure 3 of reference 10. This work was supported by NASA Glenn Research Center and funded by the NASA Office of Biological and Physical Research.

Level of Review: This material has been technically reviewed by NASA expert reviewer(s).

Available from

NASA Center for Aerospace Information
7115 Standard Drive
Hanover, MD 21076–1320

National Technical Information Service
5285 Port Royal Road
Springfield, VA 22161

Available electronically at http://gltrs.grc.nasa.gov

Hydrodynamic force on a cylinder oscillating at low frequency

Robert F. Berg
National Institute of Standards and Technology
Gaithersburg, Maryland 20899-8364

Minwu Yao and Charles H. Panzarella
Ohio Aerospace Institute
Brookpark, Ohio 44142

19 January 2005

Abstract

The hydrodynamic force on a cylinder oscillating transversely to its axis is a nonlinear function of the displacement amplitude x_0. We report measurements and numerical calculations of the force at frequencies low enough that $\delta > R$, where δ is the viscous penetration length and R is the cylinder radius. For small amplitudes, the numerically calculated Fourier transform of the force per unit length, $\hat{F}_{\rm small}$, agrees with Stokes' analytical calculation. For larger amplitudes, the force per unit length found by both calculation and measurement is $\hat{F} = \hat{F}_{\rm small} C\left(x_0/\delta, R/\delta\right)$. The complex function C depends only weakly on R/δ, indicating that x_0/δ is more appropriate as a scaling variable than the Keulegan-Carpenter number $KC = \pi x_0/R$. The measurements used a torsion oscillator driven at frequencies from 1 to 12 Hz while immersed in dense xenon. The oscillator comprised cylinders with an effective radius of $R = 13.4$ μm and oscillation amplitudes as large as $x_0/\delta = 4$ (corresponding to KC as large as 71). The calculations used similar conditions except that the amplitudes were as large as $x_0/\delta = 28$.

1 Introduction

Small transverse oscillations of a cylinder will generate a flow that is periodic and effectively two-dimensional. Describing the resulting force on the cylinder requires two independent variables because the oscillation frequency $f = \omega/2\pi$ can be varied independently of the velocity. The most frequent choices for the two variables are the Keulegan-Carpenter number,

$$KC = \pi \frac{x_0}{R}, \tag{1}$$

which compares the oscillation amplitude x_0 to the cylinder radius R, and the Stokes viscous parameter,

$$\beta = \frac{4}{\pi} \left(\frac{R}{\delta} \right)^2, \tag{2}$$

which compares the cylinder radius to the viscous penetration length defined by

$$\delta = \sqrt{\frac{2\eta}{\rho\omega}}, \tag{3}$$

where η and ρ are the viscosity and density.

The chief result of this paper is that, when $\delta > R$ (or $\beta < 1$), the scaling variable most appropriate for describing the hydrodynamic nonlinearity is the reduced length

$$\frac{x_0}{\delta} = \sqrt{\frac{\beta}{4\pi}} KC. \tag{4}$$

This choice minimizes the dependence on the second variable. We support this result with a simple scaling argument, numerical calculations, and experimental measurements. Figure 1 indicates the previously unexplored region of KC and β spanned by the present measurements and shows the locations of several familiar oscillators.

This work was made in preparation for an experiment, called "Critical Viscosity of Xenon" (CVX-2), that measured the shear thinning predicted to occur near the liquid-vapor critical point [15]. Shear thinning caused the response of the CVX-2 viscometer to be nonlinear, but the convective term of the Navier-Stokes equation caused a much larger nonlinearity [16]. To understand the larger nonlinearity we calculated and measured the oscillator's response when the xenon was far from the critical point and had no shear thinning.

CVX-2 flew on board Space Shuttle Columbia in 2003. The microgravity in Earth orbit was necessary to obtain the homogeneity of density and temperature sufficient to observe shear thinning. For the forseeable future, the CVX-2 results will likely be the only data on shear thinning in a simple pure fluid. Correctly interpreting those data, as well as addressing the classic problem of an oscillating cylinder, motivated the present study.

The experimental frequencies used by CVX-2 (1 to 12 Hz) corresponded to $\delta > R$ (or $\beta < 1$). With one exception [11], previous investigations dealing with the force on the cylinder, the surrounding flow patterns, or both [1, 2, 3, 4, 5, 6, 7, 8, 9, 10] have examined flows with KC similar to or smaller than those used here, but the values of β were always much larger than 1. (The steady streaming induced by an oscillating cylinder is not addressed here.) Large values of β occur in practical applications such as pilings for oil drilling platforms, and

they are compatible with the usual boundary-layer assumption that $\delta \ll R$. In contrast, the present results are in the range $0.01 < \beta < 0.2$, which means that $\delta > R$.

The exception is the numerical work by Morfey and Tan [11], which examined the range $10^{-6} \leq \beta \leq 0.3$. Their calculations were motivated by the attenuation of large-amplitude sound in fibrous blankets. More discussion?

Figure 1 can be related to the flow visualization study by Tatsuno and Bearman [10]. In the range defined by $1.6 < KC < 15$ and $5 < \beta < 160$ they found eight regimes of flow patterns. Only two regimes, which they called A and A^*, were two-dimensional. Figure 2 shows that the curve $x_0/\delta = 7$ approximately bounds regimes A and A^*. As shown in Figure 1, an extrapolation of that boundary to small β indicates that the present experimental results were obtained within the two-dimensional regime.

This paper studies the viscous force per unit length $F(t)$ that opposes the motion of a cylinder whose time dependent displacement is

$$x(t) = \mathrm{Re}\left[x_0 e^{i\omega t}\right]. \tag{5}$$

For small amplitudes, the Navier-Stokes equation reduces to the unsteady Stokes equation, and the force is periodic and proportional to x_0. The proportionality allows the $F(t)$ to be written as the product of the fluid mass per unit length displaced by the oscillator $\pi R^2 \rho$, the oscillator's acceleration amplitude $\omega^2 x_0$, and a dimensionless reduced force $B(R/\delta)$ as

follows [12].

$$F(t) \equiv \mathrm{Re}\left[\hat{F}_{\mathrm{small}}(f)\, e^{i\omega t}\right] = \mathrm{Re}\left[-i\left(\pi R^2 \rho \omega^2 x_0\right) B\left(\frac{R}{\delta}\right) e^{i\omega t}\right] \tag{6}$$

This form is convenient for an oscillator used as a viscometer because δ can be varied by changing the frequency while the oscillator is immersed in a fluid of known density and viscosity. The choice of R used in $B(R/\delta)$ is arbitrary; therefore, measuring the Fourier transform $\hat{F}_{\mathrm{small}}(f)$ while varying the frequency yields the calibration function $B(R/\delta)$ without knowledge of the oscillator's geometry. Figure 3 shows the magnitude and phase of $B(R/\delta)$ measured for the present experimental oscillator at small amplitudes [13]. Also shown is Stokes' solution for a cylinder with a *circular* cross section. Its modern formulation [14] is

$$B_{\mathrm{cyl}}\left(\frac{R}{\delta}\right) = -(k' + ik) = i\left[1 + \frac{4K_1(z)}{zK_0(z)}\right], \tag{7}$$

where $K_n(z)$ is the modified Bessel function of order n, and $z \equiv (1+i)(R/\delta)$. Here and in the remainder of this paper, we will use R/δ instead of β to make clear the role of δ.

For moderate amplitudes, the flow remains periodic, but the force on the cylinder is no longer proportional to x_0. Therefore we generalized Eq.(6) by multiplying the reduced force B by a complex function C that depends on reduced amplitude x_0/δ as well as R/δ.

$$\hat{F}(f) = \hat{F}_{\mathrm{small}}(f)\, C\left(\frac{x_0}{\delta}, \frac{R}{\delta}\right) \tag{8}$$

The amplitude function C, which describes our numerical and experimental results, is written as a function of x_0/δ instead of KC. Figure 4 illustrates how choosing x_0/δ for the first variable minimizes the dependence on the second variable R/δ. The magnitude and phase of C numerically calculated for a circular cylinder are each described approximately by a single function of x_0/δ.

The following section describes a simple analytical argument that supports the importance of x_0/δ as a scaling variable. Following that is a section that describes numerical calculations for the force on an oscillating circular cylinder. The final section compares the experimental measurements to the numerical results.

2 Scaling of the Navier-Stokes equation

Imagine a solid body that oscillates in an incompressible fluid according to $x(t) = x_0 \cos(\omega t)$. For small amplitudes x_0, the velocity $\mathbf{u}$ and pressure p will be periodic everywhere in the fluid. For moderately larger x_0, the velocity and pressure will remain periodic, even though harmonics and steady streaming may appear. Because there is a obvious time scale ω^{-1} one can define dimensionless time, velocity, pressure, and spatial derivatives as follows.

$$t_* \equiv \omega t \tag{9a}$$

$$\mathbf{u}_* \equiv \mathbf{u}/(\omega x_0) \tag{9b}$$

$$p_* \equiv \frac{L}{\eta \omega x_0} p \tag{9c}$$

$$\boldsymbol{\nabla}_* \equiv L\boldsymbol{\nabla} \text{ and } \boldsymbol{\nabla}_*^2 \equiv L^2 \boldsymbol{\nabla}^2 \tag{9d}$$

Here $*$ indicates the dimensionless quantities. The characteristic length L is not yet identified, which precludes its use in a viscous time scale such as $\rho L^2/\eta$; doing so leads to an ambiguous result. In terms of these dimensionless quantities, the Navier-Stokes equation is

$$\frac{\partial \mathbf{u}_*}{\partial t_*} + \frac{x_0}{L}\left(\mathbf{u}_* \cdot \boldsymbol{\nabla}_*\right)\mathbf{u}_* = -\frac{\delta}{2L^2}\boldsymbol{\nabla}_* p_* + \frac{\delta}{2L^2}\boldsymbol{\nabla}_*^2 \mathbf{u}_*. \tag{10}$$

This equation can be expressed in terms of a single dimensionless scaling variable by requiring that

$$L \equiv \delta f_L\left(\frac{x_0}{\delta}\right), \tag{11}$$

where $f_L\left(x_0/\delta\right)$ is an arbitrary function of x_0/δ. The simplest choice, $L = \delta$, puts the Navier-Stokes equation into the form

$$\frac{\partial \mathbf{u}_*}{\partial t_*} + \left(\frac{x_0}{\delta}\right)\left(\mathbf{u}_* \cdot \boldsymbol{\nabla}_*\right)\mathbf{u}_* = \frac{1}{2}\left[-\boldsymbol{\nabla}_* p_* + \boldsymbol{\nabla}_*^2 \mathbf{u}_*\right]. \tag{12}$$

Eq.(12) shows that the Navier-Stokes equation for a periodic flow can be scaled by the reduced amplitude x_0/δ if the scales chosen for time and length are respectively ω^{-1} and δ. Note that x_0/δ is equivalent to an "oscillatory Reynolds number" whose characteristic velocity and length are respectively ωx_0 and $\delta/2$. Similar Reynolds number have been used in discussions of streaming from oscillating bodies [17, 18].

3 Calculations

3.1 Numerical model

The numerical model calculated the force on the experimental oscillator, which was constructed from a screen comprising many wires of noncircular cross section. (See Figure 5 and the Measurements section.) Four simplifications were used. First, we assumed that the oscillator behaved as an assembly of isolated wires and therefore could be represented by a single cylinder oscillating transversely to its axis. This approximation was reasonable because the spacing between adjacent wires was much larger than the viscous penetration length. Second, we assumed that the cross section of the wire could be represented by a circle of appropriate diameter. Although Figure 5 shows that the actual cross section of the screen wire was closer to a rectangle, numerical studies, illustrated in Figure 6, showed that the effect of the cross-section shape was small. These first two simplifications reduced the model to the classical flow problem of a rigid circular cylinder, surrounded by an otherwise stationary incompressible Newtonian fluid, and oscillating sinusoidally in a direction normal to its axis. See Figure 7.

The third simplification assumed that the flow field was two-dimensional. An example of three-dimensional flow is Tatsuno and Bearman's regime B, where counter-rotating vortices appear alternately along the cylinder axis [10]. The fourth simplification assumed that the flow field had reflection symmetry about the oscillation direction. Both simplifications were consistent with the patterns seen in Tatsuno and Bearman's flow regimes A and A^*, although the extrapolated boundary in Figure 1 suggests that real flows with $x_0/\delta > 7$ may

be three-dimensional.

The values of density ($\rho = 1116$ kg·m^{-3}) and viscosity ($\eta = 52$ μPa·s) were similar to those of the experimental measurements. (Some test calculations used $\eta = 72$ μPa·s.) The value of the cylinder radius ($R = 13.4$ μm) was similar to the half width of a single screen wire. The range of oscillation frequencies, $0.5 \leq f \leq 12$ Hz, included the experimental frequencies, but the largest amplitude of $x_0 = 1000$ μm exceeded the experimental amplitude at all frequencies.

We used the moving reference frame approach described in Appendix A to handle the oscillatory motion of the cylinder. This approach transforms the original moving boundary problem into a fixed domain problem in which the cylinder is stationary and surrounded by oscillating fluid. To find the force $F(t)$ on the cylinder in the laboratory reference frame, we first computed the corresponding force $F'(t)$ in the moving reference frame. We then removed the spurious force due to the non-inertial frame by applying the correction prescribed in Eq.(33). The moving reference frame eliminates the need for re-meshing at each time step. In a stationary reference frame, the re-meshing cannot prevent distortion of the mesh, and the distortion at large oscillation amplitude makes convergence of the solution difficult.

3.2 Numerical Techniques

The fourth simplification mentioned above assumed that the solution had reflection symmetry about the laboratory x-axis passing through a diameter of the cylinder. Consequently,

the computational flow domain included only the upper half of the actual flow field defined by the width $-w \leq x' \leq w$, the height $0 \leq y' \leq h$, and the top half surface of the circle. The computational domain and the boundary conditions are depicted in Figure 7. The size of the computational domain was $w = h = 2000R$ for all of the oscillation frequencies and amplitudes.

The governing equations in the moving reference frame were solved using POLYFLOW [19], a commercial finite element method (FEM) program designed primarily for laminar, viscous flows involving complex rheology and free surfaces. Details of the FEM formulation and numerical techniques used in POLYFLOW are documented in [20]. Galerkin's method was adopted in the FEM discretization for the momentum equations, and the two-dimensional FEM mesh was built with 9-node, quadratic, quadrilateral elements, in which the velocity was approximated by quadratic shape functions. The pressure was approximated as piecewise-linear and discontinuous on inter-element boundaries.

No-slip boundary conditions were used at the cylinder surface. Fine grading of the mesh was necessary near the cylinder due to the strong radial dependences of velocity and stress in that region. Numerical studies of those dependences led us to give the FEM mesh elements next to the cylinder the small size $\Delta_1 = R/158$. The mesh grading away from the cylinder surface was controlled by fixing the ratio q of successive element sizes, defined as

$$q \equiv \Delta_j / \Delta_{j+1} = 0.6. \tag{13}$$

Here Δ_j is the characteristic length of element j, and j increases with radial distance from

the cylinder. Figure 8 illustrates the mesh grading.

The transient problem was solved by a predictor-corrector time integration scheme in which the second-order Crank-Nicholson method was selected for the corrector. At each time step, the non-linear algebraic system resulting from the FEM discretization was solved by the Newton-Raphson iteration scheme. Termination of the nonlinear iteration was controlled by an iteration convergence tolerance of 10^{-4} for the relative error norms of the residuals of the governing equations. For each simulation, we calculated the transient solution for 600 time steps, yielding a total of 6 complete oscillation cycles. Steady state was achieved after 4 complete oscillation cycles, so the fifth and sixth oscillation cycles were used to determine the Fourier coefficients of the force on the cylinder.

The velocity $u_0 = x_0\omega\sin(\omega t)$ imposed at the domain boundaries was sinusoidal at frequency ω. However, the resulting force on the cylinder $F(t)$, after correcting for the moving reference frame, contained harmonics for large amplitudes x_0.

$$F(t) = a_0 + \sum_{n=1}^{\infty} \left[b_n \cos(n\omega t) - a_n \sin(n\omega t) \right], \tag{14}$$

Several recent analyses [21, 22, 23, 24, 25, 26] of large-amplitude shear viscometry decomposed the non-linear force into a series of harmonic functions in a similar manner. The discrete Fourier analysis of $F(t)$ was transformed into a general linear least-squares curve fitting problem and solved using the singular value decomposition algorithm described in [27]. A total of 41 terms in Eq.(14) were used to fit the Fourier coefficients a_n and b_n with $n = 0, 1, \cdots, 20$. Numerical tests indicated that the accuracy of the Fourier coefficients

fitted by the singular value decomposition algorithm was satisfactory. This paper discusses the results at only the fundamental frequency ($n = 1$) because the harmonics were small. The magnitude at 3ω never exceeded 7 % of that at ω, and the magnitudes of higher odd harmonics were 1 % or smaller. The magnitudes for all even harmonics ($2\omega, 4\omega, ...$) were insignificant.

3.3 Validation

When $x_0 \ll R$, the force on the oscillating circular cylinder can be calculated with Stokes' analytical solution. If the cylinder moves according to $x(t) = x_0 \cos(\omega t)$, the opposing force per unit length is

$$F(t) = -a_1 \sin(\omega t) + b_1 \cos(\omega t) = \mathrm{Re}\left[(b_1 + i a_1) e^{i\omega t}\right], \tag{15}$$

where

$$\frac{a_1}{\pi R^2 \rho \omega^2 x_0} = \mathrm{Re}\left[B_{\mathrm{cyl}}\right] \qquad \text{and} \qquad \frac{b_1}{\pi R^2 \rho \omega^2 x_0} = -\,\mathrm{Im}\left[B_{\mathrm{cyl}}\right]. \tag{16}$$

We estimated the accuracy of the numerical solutions at small amplitude by comparing them with the analytical solutions. Table 1 shows example results for three values of the mesh grading ratio q. The value $q = 0.60$ reduced the errors for a_1 and b_1 to less than 0.06 % of the magnitude for all frequencies. (Fortuitous cancellations made the magnitude errors even smaller.)

Table 1. Small-amplitude comparisons between Stokes' analytical solution and numerical solutions using three mesh grading ratios q. The Fourier coefficients a_1 and b_1 of the force on the circular cylinder were calculated for $\rho = 1116$ kg/m^3 and $\eta = 72$ μPa·s at $f = 1$ Hz. The cylinder radius and oscillation amplitude were 13.4 μm and 1 μm respectively. The errors are relative to the magnitude $\sqrt{a_1^2 + b_1^2}$.

mesh	$\mathbf{a_1 \times 10^6}$	**error**	$\mathbf{b_1 \times 10^6}$	**error**	$\mathbf{\sqrt{a_1^2 + b_1^2} \times 10^6}$	**error**
$q = 0.80$	–2.38163	1.18 %	0.835909	1.01 %	2.52407	1.45 %
$q = 0.65$	–2.35201	–0.01 %	0.810190	–0.03 %	2.48764	–0.02 %
$q = 0.60$	–2.35270	0.02 %	0.810376	–0.02 %	2.48836	0.01 %
Stokes solution	**–2.35227**		**0.810815**		**2.48809**	

The effect of mesh grading was studied at large amplitude also. Table 2 compares the result for $q = 0.60$ to those obtained for coarser meshes. As with the small-amplitude comparisons, the results are nearly independent of q for $q \leq 0.65$. The present results were obtained with $q = 0.60$, so the uncertainty due to that mesh size is likely less than 0.1 %.

Table 2. Large-amplitude comparisons between numerical solutions using three mesh grading ratios q. The Fourier coefficients a_1 and b_1 of the force on the circular cylinder were calculated for $\eta = 52$ μPa·s at $f = 12$ Hz and $x_0 = 1000$ μm. The differences from the $q = 0.60$ result are relative to the magnitude $\sqrt{a_1^2 + b_1^2}$.

mesh	$\mathbf{a_1 \times 10^6}$	**difference**	$\mathbf{b_1 \times 10^6}$	**difference**	$\mathbf{\sqrt{a_1^2 + b_1^2} \times 10^6}$	**difference**
$q = 0.80$	–139.0283	8.76 %	43.01326	8.92 %	145.5301	10.82 %
$q = 0.65$	–127.4870	–0.03 %	31.14365	–0.13 %	131.2359	–0.06 %
$q = 0.625$	–127.4856	–0.03 %	31.21592	–0.07 %	131.2517	0.05 %
$\mathbf{q = 0.60}$	**–127.5294**		**31.30997**		**131.3166**	

The effect of domain size was studied by truncating the domain lengths L and H from $2000R$ to $500R$. At $f = 1$ Hz and $x_0 = 1000$ μm, the reduction changed a_1 and b_1 by only 0.02 %.

3.4 Numerical results

Figure 9 shows examples of the flow field near the cylinder at three oscillation amplitudes x_0. The contours show constant values of the shear component of the rate-of-deformation tensor, defined as $D_{xy} = \left(\partial u/\partial y' + \partial v/\partial x'\right)/2$, where u and v are the velocity components in the x' and y' directions.1

Tables 3 and 4 give the magnitude and phase of the Fourier-transformed force per unit length $\hat{F}(f) = b_1 + ia_1$ normalized by $\pi R^2 \rho \omega^2 x_0$. The ranges of frequency and amplitude include the experimental values.

Table 3. Magnitude of $\hat{F}(f) / (\pi R^2 \rho \omega^2 x_0)$ computed for $R = 13.4$ μm, $\rho = 1116$ kg·m^3, $\eta = 52$ μPa·s.

x_0 (μm)	**0.5 Hz**	**1 Hz**	**3 Hz**	**5 Hz**	**8 Hz**	**12 Hz**
1	134.499	77.407	33.529	23.180	16.725	12.766
10	134.511	77.422	33.549	23.203	16.751	12.795
60	134.942	77.940	34.233	23.972	17.596	13.700
100	135.714	78.849	35.360	25.174	18.836	14.942
200	139.056	82.545	39.199	28.850	22.267	18.121
400	149.271	92.251	47.068	35.770	28.386	23.638
600	160.662	101.913	54.122	41.842	33.702	28.405
800	171.754	110.942	60.534	47.337	38.501	32.699
1000	182.308	119.391	66.477	52.429	42.955	36.692

Table 4. Phase of $\hat{F}(f)$ in radians.

x_0 (μm)	0.5 Hz	1 Hz	3 Hz	5 Hz	8 Hz	12 Hz
1	-1.2592	-1.2196	-1.1407	-1.0964	-1.0509	-1.0079
10	-1.2593	-1.2198	-1.1414	-1.0976	-1.0530	-1.0111
60	-1.2626	-1.2268	-1.1638	-1.1346	-1.1093	-1.0889
100	-1.2682	-1.2383	-1.1945	-1.1778	-1.1635	-1.1496
200	-1.2901	-1.2768	-1.2623	-1.2520	-1.2365	-1.2166
400	-1.3391	-1.3387	-1.3249	-1.3078	-1.2846	-1.2596
600	-1.3736	-1.3726	-1.3526	-1.3329	-1.3097	-1.2880
800	-1.3963	-1.3934	-1.3701	-1.3507	-1.3298	-1.3113
1000	-1.4122	-1.4078	-1.3836	-1.3656	-1.3468	-1.3300

We now use the amplitude function $C(x_0/\delta, R/\delta)$ to plot the numerical results. Combining Eqs.(6) and (8) gives

$$C \equiv |C| e^{i\phi} = \frac{\left(\hat{F}/x_0\right)}{\lim_{x_0 \to 0}\left(\hat{F}/x_0\right)} = \frac{(b_1 + ia_1)_{x_0}}{x_0} \frac{1\ \mu\text{m}}{(b_1 + ia_1)_{1\ \mu\text{m}}}. \tag{17}$$

Dividing the ratio $\hat{F}/x_0$ calculated at amplitude x_0 by the ratio calculated at the smallest amplitude of 1 μm gives the magnitude and phase of C. Figure 4 plots $|C|$ and ϕ as functions of reduced amplitude. The points have some scatter because R/δ varied by a factor of $\sqrt{24}$ when the frequency was varied from 0.5 Hz to 12 Hz. The relatively small scatter shows that the dependence of C on R/δ is weak.

We obtained a correction for the dependence of C on R/δ that allowed better comparisons between the results at different frequencies. This was done by reducing R from 13.4 μm to 6.7 μm and repeating the 5 Hz calculations. The reduction of R caused small decreases of both $|C|$ and ϕ, which allowed us to estimate the derivatives $d|C|/dR$ and $d\phi/dR$. Figure 10 shows that plotting these derivatives as functions of x_0/δ suggests empirical forms for the dependence of C on R/δ.

The plot of $d|C|/dR$ showed that the dependence of $|C|$ on R/δ could be approximately described by

$$\frac{1}{|C|}\frac{\partial|C|}{\partial(R/\delta)} \simeq \frac{|C|-1}{2}. \tag{18}$$

Solving this differential equation yields

$$\left|C\left(\frac{x_0}{\delta},\frac{R}{\delta}\right)\right| = \left[1 - C_0\left(\frac{x_0}{\delta}\right)\exp\left(\frac{R}{2\delta}\right)\right]^{-1}, \tag{19}$$

where $C_0(x_0/\delta)$ is an undetermined function. Similarly, the plot of ϕ showed that the dependence of ϕ on R/δ could be approximately described by

$$\frac{\partial\phi}{\partial(R/\delta)} \simeq \phi. \tag{20}$$

Solving for ϕ yields

$$\phi\left(\frac{x_0}{\delta},\frac{R}{\delta}\right) = C_\phi\left(\frac{x_0}{\delta}\right)\exp\left(\frac{R}{\delta}\right), \tag{21}$$

where $C_\phi(x_0/\delta)$ is an undetermined function.

Eqs.(19) and (21) use known functions of R/δ to describe the dependence of C on R/δ. Therefore, the value of C calculated (or measured) for an oscillating cylinder of reduced amplitude x_0/δ and reduced radius R/δ can be adjusted to the value of C expected at the same x_0/δ but different R/δ. This adjustment is useful because it allows a calculation of C

obtained at one frequency to be compared to a calculation obtained at a different frequency by adjusting the calculations to a common "reference" value $(R/\delta)_{\text{ref}}$. The most convenient reference is $(R/\delta)_{\text{ref}} = 0$, which corresponds to the limit of infinitesimally small radius or, equivalently, infinitesimally small frequency. The following equations adjust $C(x_0/\delta, R/\delta)$ to $C(x_0/\delta, 0)$.

$$\left|C\left(\frac{x_0}{\delta}, 0\right)\right| = \left\{1 - \left[1 - \frac{1}{|C(x_0/\delta, R/\delta)|}\right] \exp\left(-\frac{R}{2\delta}\right)\right\}^{-1} \tag{22a}$$

$$\phi\left(\frac{x_0}{\delta}, 0\right) = \phi\left(\frac{x_0}{\delta}, \frac{R}{\delta}\right) \exp\left(-\frac{R}{\delta}\right) \tag{22b}$$

Figure 11 uses Eq.(22) to plot the magnitude and phase of $C(x_0/\delta, 0)$ as a function of x_0/δ. Using $(R/\delta)_{\text{ref}} = 0$ improved the consistency of the results for $x_0/\delta < 10$, especially in the phase. For larger x_0/δ, the magnitude results are inconsistent by as much as 3 %. The cause of this remaining inconsistency may be due to the approximations in Eqs.(18) and (20). It is worth noting that, as indicated in Figure 1, the data for $x_0/\delta > 7$ lie outside the boundary extrapolated from Tatsuno & Bearman's regimes A and A^*.

Note the initial quadratic behavior of $|C|$ and ϕ in Figures 4 and 11. Such behavior is expected because an expansion of C about $x_0/\delta = 0$ must include only terms even in x_0/δ; otherwise the value of C would depend on the sign of x_0. The initial quadratic behavior was built into the curves drawn in Figure 11. These empirical descriptions of the numerical

results are given by Eq.(23), where $b_0 = 4.3$, $c_0 = 36$, $a_\phi = 4$, $b_\phi = 3.5$, and $c_\phi = 36$.

$$\left|C\left(\frac{x_0}{\delta}, 0\right)\right| \simeq 1 + \left[\frac{b_0}{(x_0/\delta)^{1/2}} + \frac{c_0}{(x_0/\delta)^2}\right]^{-1} \tag{23a}$$

$$\phi\left(\frac{x_0}{\delta}, 0\right) \simeq -\left[a_\phi + \frac{b_\phi}{(x_0/\delta)^{1/2}} + \frac{c_\phi}{(x_0/\delta)^2}\right]^{-1} \tag{23b}$$

4 Measurements

4.1 Experimental method

The oscillator and xenon sample were the same as for the CVX experiment [13]. The density was fixed at xenon's critical density ($\rho = 1116$ kg·m^{-3}) by sealing the sample cell, and the viscosity was fixed near $\eta = 52$ μPa·s by controlling the temperature near 295 K. A brief description of the apparatus is given below, and a detailed description can be found in [13]. A later publication will describe the electronic modifications made for CVX-2 that allowed operation at large x_0 [16].

Figure 5 indicates the geometry of the oscillator. The oscillator was an 8×19 mm rectangle of screen that was cut out of a larger piece of nickel screen. The screen consisted of a square grid of wires formed by electrodeposition. When the screen was cut, one wire was left extending from the middle of both of the rectangle's long edges. These two extensions served as torsion springs, and they were soldered to a stiff yoke that was centered between four electrodes placed parallel to the screen. While immersed in the xenon, the screen was driven to oscillate much like a child's seesaw.

The viscous penetration length was always in the range 35 μm $< \delta <$ 122 μm. Thus δ was larger than the width of a screen wire (30 μm), but much less than the distance between wires (847 μm). Figure 5 shows that the cross section of a typical screen wire was approximately an 8×30 μm rectangle. Despite the wire's noncircular cross section, Figure 3 shows that the drag on the screen resembled that of an assembly of isolated circular cylinders. Using the value $R = 13.4$ μm in Stokes' analytical function $B_{\rm cyl}\left(R/\delta\right)$ approximately describes the experimental values obtained for $B\left(R/\delta\right)$ at small amplitude.

The oscillator was driven electrostatically at 1, 3, 5, 8, and 12 Hz. Four electrodes surrounding the oscillator (not shown in Figure 5) simultaneously applied combinations of a DC voltage $V_{\rm DC}$ and a sinusoidal voltage $V_{\rm in}\left(t\right) = V_0 \sin\left(\omega t\right)$. The resulting torque on the oscillator was

$$N\left(t\right) = K\left[\frac{V_{\rm in}\left(t\right)}{V_{\rm DC}} + \frac{x_{\rm tip}\left(t\right)}{x_{\rm gap}}\right], \tag{24}$$

where $x_{\rm tip}\left(t\right)$ is the displacement at the oscillator's tip, and $x_{\rm gap} \simeq 4$ mm is the length of the gap between the oscillator and one electrode. The dimensionless calibration factor K was adjusted so that the values of $B\left(R/\delta\right)$ obtained for small x_0 agreed with those determined earlier for the CVX experiment [13], which also were made at small x_0.

The apparatus used for the present measurements differed from the CVX experiment in that the drive voltages $V_{\rm DC}$ and $V_{\rm in}\left(t\right)$ were larger and the time dependence of $V_{\rm in}\left(t\right)$ was a single frequency instead of a frequency chirp. In particular, the second term of Eq.(24), which caused the electrostatic torque to increase linearly with the oscillator's tip displacement

$x_{\rm tip}\,(t)$, was more significant. The result was a negative contribution to the oscillator's spring constant, which the analysis handled by decreasing the oscillator's resonance frequency by approximately 1 Hz from its vacuum value of 11 Hz. Terms of order $\left(x_{\rm tip}\,(t)\,/x_{\rm gap}\right)^2$ and higher were not included in Eq.(24) because the oscillator's small amplitude and the approximate symmetry of the electrode pairs made them negligible.

The oscillator's time-dependent angular displacement $\theta\,(t)$ was detected by the unbalance of a capacitance bridge operating at 10 kHz. The out-of-balance signal was fed to a lock-in amplifier, which generated a voltage whose oscillating component $V_{\rm out}\,(t)$ was proportional to $\theta\,(t)$:

$$\theta\,(t) = \theta_0 \cos\left(\omega t\right) = \frac{1}{r_{\rm tip}} \left(\frac{dx_{\rm tip}}{dV_{\rm out}}\right) V_{\rm out}\,(t)\,. \tag{25}$$

Here, $r_{\rm tip}$ is the distance from the torsion axis to the oscillator's tip. Video images of the oscillator were used to measure the derivative $dx_{\rm tip}/dV_{\rm out} = (53.1 \pm 1.2)\ \mu$m/V. The resolution of the images dominated the uncertainty of this result.

The oscillator's response was defined as the Fourier transform $\hat{\theta}\,(f)$ of the angular displacement divided by the Fourier transform $\hat{N}\,(f)$ of the applied torque.

$$G\,(f, \theta_0) = \frac{\hat{\theta}\,(f)}{\hat{N}\,(f)} = \frac{K}{r_{\rm tip}} \left(\frac{dx_{\rm tip}}{dV_{\rm out}}\right) \frac{\hat{V}_{\rm out}\,(f)}{\hat{V}_{\rm in}\,(f)} \tag{26}$$

Here $\hat{V}_{\rm in}\,(f)$ and $\hat{V}_{\rm out}\,(f)$ are the Fourier transforms of the input and output voltages. (For clarity, Eqs. (24) and (25) do not show the frequency-dependent corrections that account

for the anelasticity of the oscillator's spring constant and the gain and phase shifts of the drive and detection circuits.)

The amplitude V_0 and frequency f of the AC drive voltage determined the oscillation amplitude x_0. A determination of the hydrodynamic force at amplitude x_0 comprised two measurements. The first measurement used a drive torque sufficiently small that $C = 1$. (Its amplitude of 1.1×10^{-10} N·m was approximately that used in the small-amplitude CVX experiment [13].) The second measurement used a torque that was larger by a factor of either 20 or 33 to produce the oscillation amplitude x_0. Due to the oscillator's response, the largest value of x_0/δ was achieved at 3 Hz. Figure 12 indicates the sizes of x_0 and δ at 3 Hz relative to the wire cross section.

The present measurements were made sufficiently far above the critical temperature of 290 K that density stratification and internal waves were negligible. The viscosity was always within 1% of the value used in the numerical calculations.

4.2 Experimental analysis and results

Each of the many wires comprised by the screen moved at a speed that depended on its distance from the torsion axis. We focused on the wire located at the oscillator tip, whose displacement was

$$x_{\mathrm{tip}}(t) = \theta_0 r_{\mathrm{tip}} \cos(\omega t) = x_0 \cos(\omega t) . \tag{27}$$

Comparing the experimental data to the numerical calculations at amplitude x_0 required five steps.

1. Eq.(34) in Appendix B was solved to convert the measured response $G(f, \theta_0)$ to values of $B_{\text{osc}}(R/\delta, \theta_0)$, which describes the hydrodynamics of the entire oscillator. Nonlinearity of the capacitive drive and detection required a correction that did not exceed 1.3 % of $|G|$.

2. Eq.(37) in Appendix B was used to convert $B_{\text{osc}}(R/\delta, \theta_0)$ and its derivative with respect to θ_0 into the product $[BC]_{\text{exp}}$ that described the hydrodynamics of the oscillator tip. The value of B_{osc} could not be compared directly to the numerical calculations because the total torque on the oscillator was the weighted sum of torques from all parts of the oscillator.

3. The value of C at the oscillator tip was obtained by dividing $[BC]_{\text{exp}}$ by $B(R/\delta)$ as follows.

$$C\left(\frac{x_0}{\delta}, \frac{R}{\delta}\right) = \frac{[B(R/\delta)\, C(x_0/\delta, R/\delta)]_{\text{exp}}}{B(R/\delta)} \tag{28}$$

   This approximated $B(R/\delta)$ for a single wire by the experimental value for the entire oscillator $B_{\text{osc}}(R/\delta, \theta_0)$ measured at sufficiently small θ_0. This approximation was accurate because the value of θ_0 used to determine $B(R/\delta)$ corresponded to $x_0/\delta < 0.1$.

4. The value of C was corrected for the noncircular shape of the wire's cross section, which was modeled as a rectangle with quarter-circle ends (30 μm width, 8 μm radii).

The inset of Figure 6 indicates this shape, and the data show that the numerically calculated differences in C due to shape are small (about 1 % at the experimental maximum $x_0/\delta = 4$). The correction comprised interpolating functions fitted to the magnitude and phase data shown in Figure 6. The resulting values of C corresponded to the numerical calculations for a circle of 13.4 μm radius.

5. The value of $C\left(x_0/\delta, R/\delta\right)$ was converted to $C\left(x_0/\delta, 0\right)$. Using the reference value $\left(R/\delta\right)_{\text{ref}} = 0$ simplifies the comparison with the calculated values of C.

Figure 13 plots the measured magnitude and phase of $C\left(x_0/\delta, 0\right)$. The abscissa is the reduced displacement amplitude $x_0/\delta = r_{\text{tip}}\theta_0/\delta$, where r_{tip} is distance of the oscillator's tip from its torsion axis. The angular oscillations were sufficiently small ($\theta_0 < 0.05$ rad) that the tip motion was always effectively rectilinear. Also shown are curves that represent the magnitude and phase of the calculated values of $C\left(x_0/\delta, 0\right)$ shown in Figure 11. The similarity of the measured and the calculated values is remarkable because the oscillator wire's actual cross section is far from circular. Clearly, the condition $\delta > R$ made the viscous force insensitive to the shape of the wire's cross section.

5 Concluding remarks

Hydrodynamic scaling, numerical calculations, and experiment all show that the reduced force C on an oscillating cylinder depends chiefly on the scaling variable x_0/δ when $\delta > R$. The dependences of C on the shape and size of the cylinder's cross section are weak. Further

work building on these results might answer the following questions.

- The scaling argument suggests that the force in a periodic flow field would scale as x_0/δ even if the field were three-dimensional. Would this be supported by measurements or three-dimensional numerical calculations?

- Eqs.(18) and (20) describe the dependence of C on R/δ over a limited range of x_0/δ. Over what ranges of R/δ and x_0/δ are these simple empirical forms valid?

- What is C for a linear viscoelastic fluid?

- Figure 1 shows that guitar strings and some insects oscillate near the boundary for two-dimensional flow approximately defined by $x_0/\delta = 7$. Why?

7 Appendix A: The moving reference frame approach

This approach allows the hydrodynamic force on the cylinder to be calculated within a (non-inertial) reference frame that moves with the oscillating cylinder. In the laboratory (inertial) reference frame, the cylinder's velocity is

$$u_0(t) = \mathrm{Re}\left[\frac{d}{dt} x_0 e^{i\omega t}\right] = -x_0\omega \sin(\omega t) \tag{29}$$

in the x-direction. At the cylinder surface, the fluid velocity is

$$\mathbf{u}_0 = (u, v) = (u_0, 0), \tag{30}$$

and far from the cylinder it is zero. Applying the velocity transformation $\mathbf{u} \equiv \mathbf{u}' + \mathbf{u}_0$ creates a moving reference frame in which the cylinder is motionless and the fluid velocity far from the cylinder is $-\mathbf{u}_0$. Applying the same velocity transformation to the Navier-Stokes equation yields

$$\rho\left(\frac{\partial \mathbf{u}'}{\partial t} + \mathbf{u}' \cdot \nabla \mathbf{u}'\right) = -\boldsymbol{\nabla}(p + p_0) + \mu \nabla^2 \mathbf{u}', \tag{31}$$

where the time-dependent pressure is

$$p_0 = \rho \frac{\partial u_0}{\partial t} x' = -\rho\omega^2 x_0 \cos(\omega t)\, x'. \tag{32}$$

Integrating p_0 over the surface of the cylinder relates the force per unit length F in the inertial reference frame to the force per unit length F' calculated in the non-inertial frame.

$$F(t) = F'(t) - \pi R^2 \rho \omega^2 x_0 \cos(\omega t) \tag{33}$$

Note that the force correction is proportional to $\pi R^2 \rho$. More generally, one can show that the force correction for an oscillating body of arbitrary shape and fixed orientation is proportional to the fluid mass displaced by the body.

8 Appendix B: Inferred force on the oscillator's tip

This appendix describes how we inferred the force on the fastest moving wire, located at the oscillator's tip, from the response of the entire oscillator. The oscillator response at large angular amplitude θ_0 can be written in a form similar to that used at small amplitudes. The following is Eq.(15) in Reference [13] but generalized to large θ_0.

$$G\left(f,\theta_0\right)=\frac{1}{k}\left[1-\left(\frac{f}{f_0}\right)^2+i\left(\frac{\rho}{\rho_s}\right)\left(\frac{f}{f_0}\right)^2 B_{\mathrm{osc}}\left(\frac{R}{\delta},\theta_0\right)\right]^{-1} \tag{34}$$

(For clarity, Eq.(34) does not show the frequency-dependent corrections for anelasticity and the experimental electronics.) Here k and f_0 are the oscillator's torsion spring constant and vacuum resonance frequency, respectively. The oscillator's effective density is $\rho_s=\rho_l/\left(\pi R^2\right)$, where ρ_l is the wire's measured linear density. The definition of ρ_s assumes that the wire's cross section is circular, unlike the actual wire. (See Figure 5.) Choosing $R=13.4$ μm made the values of B_{osc} measured at small amplitude similar to those calculated for a circular cylinder of the same radius. However, the size and shape of the assumed cross section is unimportant because it shifts only the magnitude of B_{osc}. The shift does not affect the value of C because it is independent of oscillation amplitude.

Inverting Eq.(34) yields $B_{\mathrm{osc}}\left(R/\delta,\theta_0\right)$, the dimensionless force-to-displacement ratio of the entire oscillator. Nonlinear hydrodynamics complicates the relation between θ_0 and B_{osc} because the experimental torque was a geometrically weighted sum of the local forces on individual oscillator wires. For large θ_0 the local force on an individual wire was an

unknown function of x_0, because the dependence of the amplitude function C on x_0/δ was unknown.

Because the oscillator screen comprised some 200 squares, the screen was modeled as a continuous distribution of wires. Also, θ_0 was sufficiently small (< 0.05 rad) that the local displacement x_0 was proportional to θ_0. We thus approximated $B_{\rm osc}\left(R/\delta, \theta_0\right)$ by the integral

$$B_{\rm osc}\left(\frac{R}{\delta}, \theta_0\right) \simeq \frac{3}{r_{\rm tip}} \int_0^{r_{\rm tip}} B\left(\frac{R}{\delta}\right) C\left(\frac{\theta_0 r}{\delta}, \frac{R}{\delta}\right) \left(\frac{r}{r_{\rm tip}}\right)^2 dr. \tag{35}$$

Here, r measures distance from the torsion axis at $r = 0$, and the oscillator's tip is located at $r = r_{\rm tip}$. The product BC is the reduced force on a *single* screen wire that is located at r and oscillates with a *linear* displacement amplitude $x_0 = \theta_0 r$. In the limit of small amplitude, $C = 1$, and Eq.(35) yields $B_{\rm osc}\left(R/\delta, 0\right) = B\left(R/\delta\right)$, the function used in Eq.(6).

To obtain the function that describes the oscillator's tip we first take the derivative of Eq.(35) with respect to θ_0.

$$\begin{aligned} \frac{d}{d\theta} B_{\rm osc}\left(\frac{R}{\delta}, \theta_0\right) &= \frac{3}{r_{\rm tip}} \int_0^{r_{\rm tip}} B\left(\frac{R}{\delta}\right) \left[\frac{d}{d\theta_0} C\left(\frac{\theta_0 r}{\delta}, \frac{R}{\delta}\right)\right] \left(\frac{r}{r_{\rm tip}}\right)^2 dr & \text{(36a)} \\ &= \frac{3}{r_{\rm tip}} \int_0^{r_{\rm tip}} B\left(\frac{R}{\delta}\right) \left[\frac{r}{\theta_0}\frac{d}{dr} C\left(\frac{\theta_0 r}{\delta}, \frac{R}{\delta}\right)\right] \left(\frac{r}{r_{\rm tip}}\right)^2 dr & \text{(36b)} \end{aligned}$$

Rearranging and integrating by parts yields

$$B\left(\frac{R}{\delta}\right) C\left(\frac{x_0}{\delta}, \frac{R}{\delta}\right) = B_{\rm osc}\left(\frac{R}{\delta}, \theta_0\right) + \frac{\theta_0}{3}\left[\frac{d}{d\theta_0} B_{\rm osc}\left(\frac{R}{\delta}, \theta_0\right)\right]. \tag{37}$$

Eq.(37) gives the hydrodynamics of the oscillator's tip in terms of the oscillator's force/displacement ratio and its derivative with respect θ_0.

9 Appendix C: Selected notation

Table 6. Notation used in several places.

A, A^*	Figures 1 and 2, two-dimensional flow regimes [10]
a_1, b_1	Eq.(15), Fourier components of numerically calculated force
$B\left(R/\delta\right)$	Eq.(6), dimensionless force on arbitrary cylinder at small x_0
$B_{\rm cyl}\left(R/\delta\right)$	Eq.(7), dimensionless force on circular cylinder at small x_0
$B_{\rm osc}\left(\frac{R}{\delta}, \theta_0\right)$	Eq.(34), dimensionless force on entire oscillator at amplitude θ_0
$C\left(x_0/\delta, R/\delta\right)$	Eq.(8), amplitude function
$C_0\left(x_0/\delta\right)$	Eq.(19), function that governs dependence of $\lvert C\rvert$ on x_0/δ
$C_\phi\left(x_0/\delta\right)$	Eq.(21), function that governs dependence of ϕ on x_0/δ
F	Eq.(6), force per unit length on the cylinder or wire
$\hat{F}_{\rm small}$	Eq.(6), force per unit length in the limit of small x_0
$G\left(f, \theta_0\right)$	Eqs.(26) and (34), experimental oscillator's response
h, w	Figure 7, height and half-width of computational domain
KC	Eq.(1), Keulegan-Carpenter number
L	characteristic length for oscillating flow
$r_{\rm tip}$	Eq.(25), distance between the tip and the torsion axis of the oscillator
R	radius of the cylinder or characteristic radius of the wire
u_0	velocity amplitude of the cylinder
u, v	fluid velocity components in the x and y directions
$V_{\rm in}, V_{\rm out}$	experimental input and output voltages
x_0	displacement amplitude of the cylinder
$x_{\rm tip}\left(t\right)$	displacement of the wire at the oscillator tip
x, y	coordinates in stationary reference frame
β	Eq.(2), Stokes viscous parameter
δ	Eq.(3), viscous penetration length
η	viscosity
θ_0	angular displacement amplitude of the experimental oscillator
ρ	density
ϕ	Eq.(17), phase of $C\left(x_0/\delta, R/\delta\right)$

Table 7. Modifications of some variables.

modification	**example**
dimensionless	velocity $\mathbf{u}_*$
moving reference frame	velocity $\mathbf{u}'$
Fourier transform	force $\hat{F}$

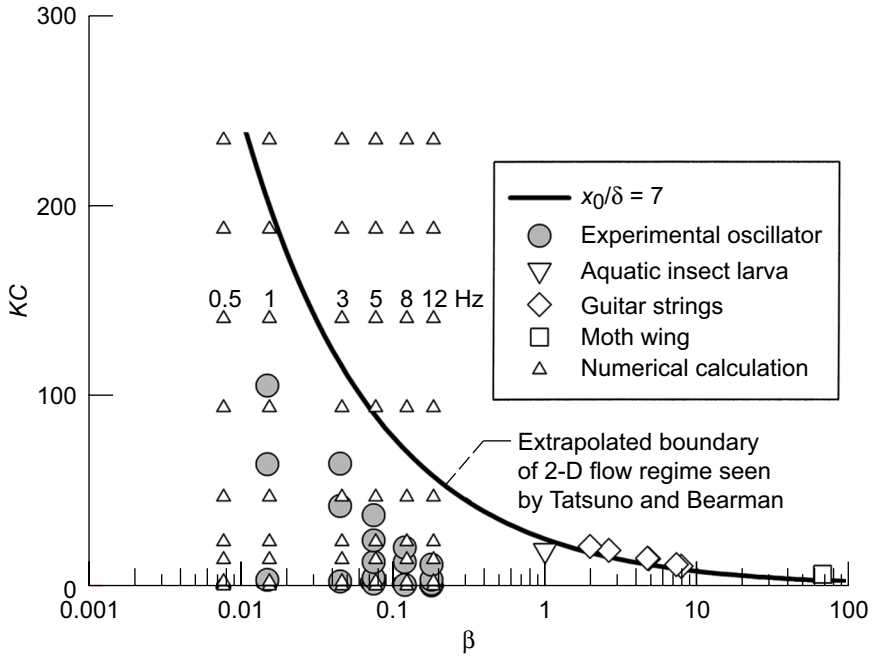

Figure 1.—Values of Keulegan-Carpenter number *KC* and viscous parameter β used in the calculations and measurements. The values for several familiar oscillators are also shown. The curve $x_0/\delta = 7$ is an extrapolation to small β of the two-dimensional flow regimes found by Tatsuno and Bearman's flow visualization study [10].

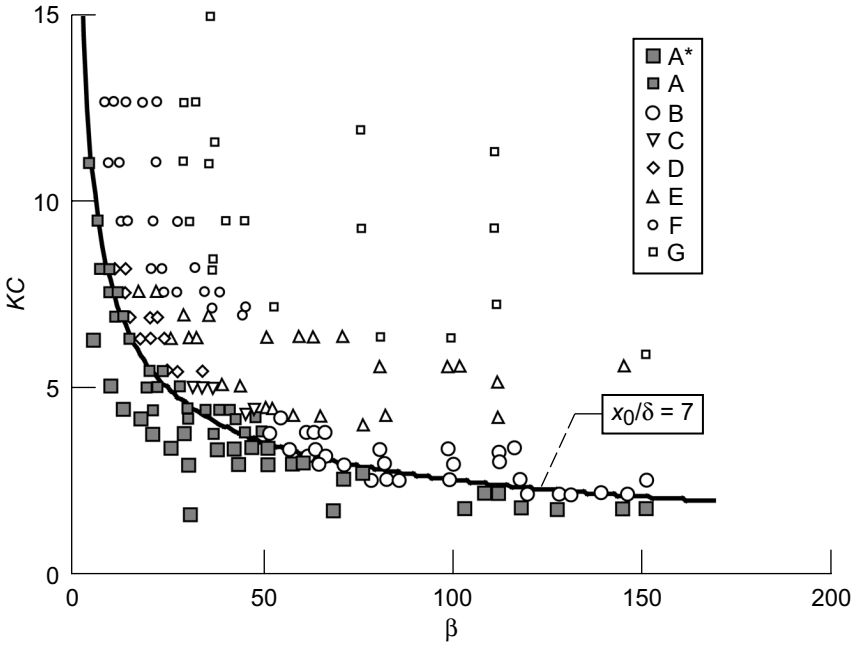

Figure 2.—Data from Figure 3 of Tatsuno and Bearman's flow visualization study [10]. The curve $x_0/\delta = 7$ approximately bounds the two-dimensional flow regimes called A and A*.

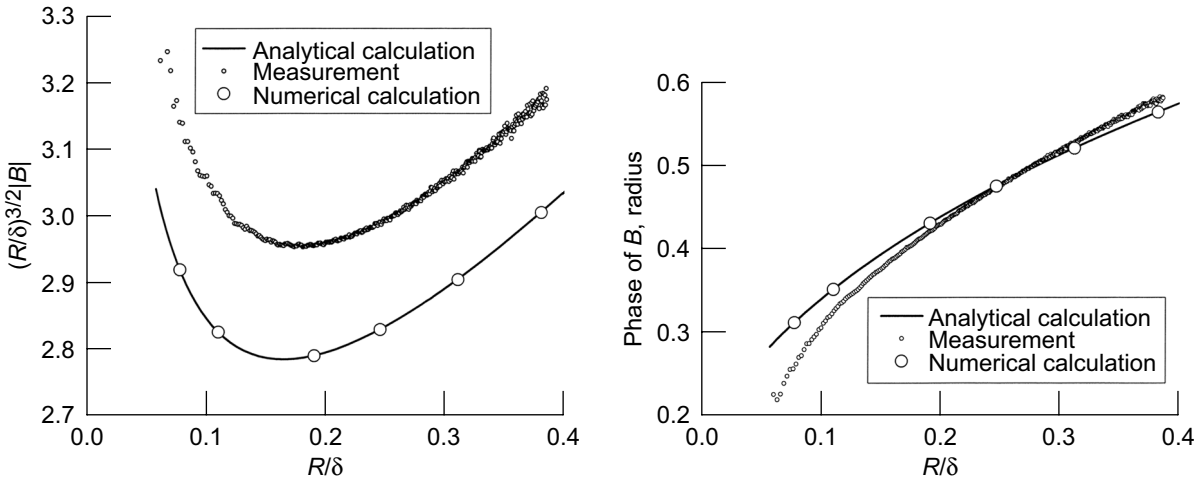

Figure 3.—Magnitude and phase of the hydrodynamic function B (R/δ) for the present oscillator measured at small amplitudes [12]. The analytical calculation is Stokes' function B_{cyl} (R/δ). Choosing R = 13.4 μm for the oscillator's effective radius brought the measured values near the calculated values. The similarity between the measured and calculated values shows that the oscillator's hydrodynamics resembled that of an assembly of isolated circular cylinders. (upper) Magnitude scaled to reveal departures from the dominant $(R/\delta)^{3/2}$ behavior. The offset of the measured values is unimportant because it corresponds to an error of only 6% in the linear mass density of a single wire. (The nominal density was estimated by weighing a piece of screen different from that used to make the oscillator.)

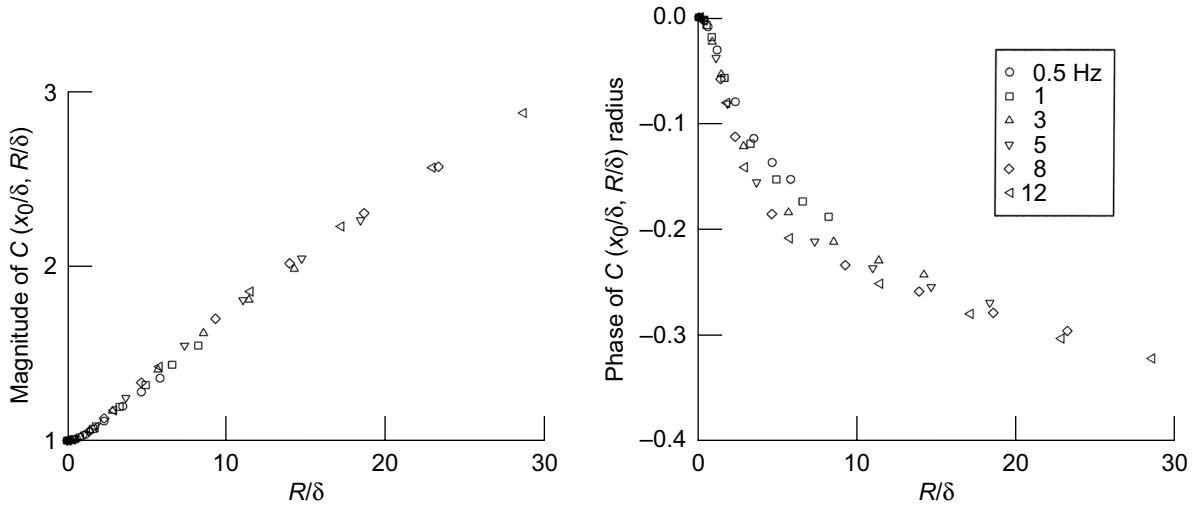

Figure 4.—Numerically calculated magnitude and phase of the amplitude function C (x_0/δ, R/δ) as a function of reduced amplitude. The dependence of C on x_0/δ is approximately independent of frequency even though R/δ varies by a factor of $\sqrt{24}$.

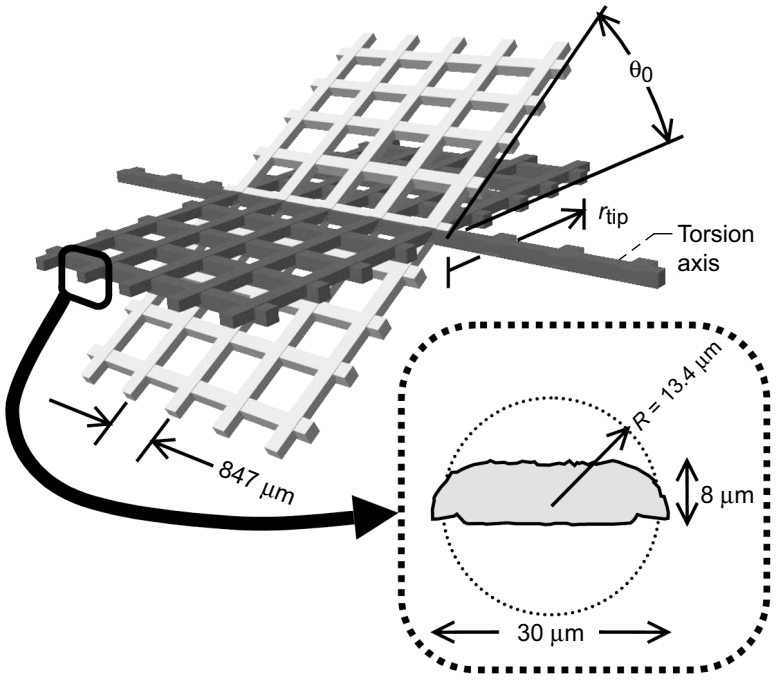

Figure 5.—Schematic diagram of the oscillator (not to scale). The oscillator's torsional displacement θ_0 caused the local displacement amplitude $x_0 = r\theta_0$, where r is the distance from the torsion axis. The inset shows the cross section of a typical oscillator wire superposed over the circular radius R = 13.4 μm used by the calculation.

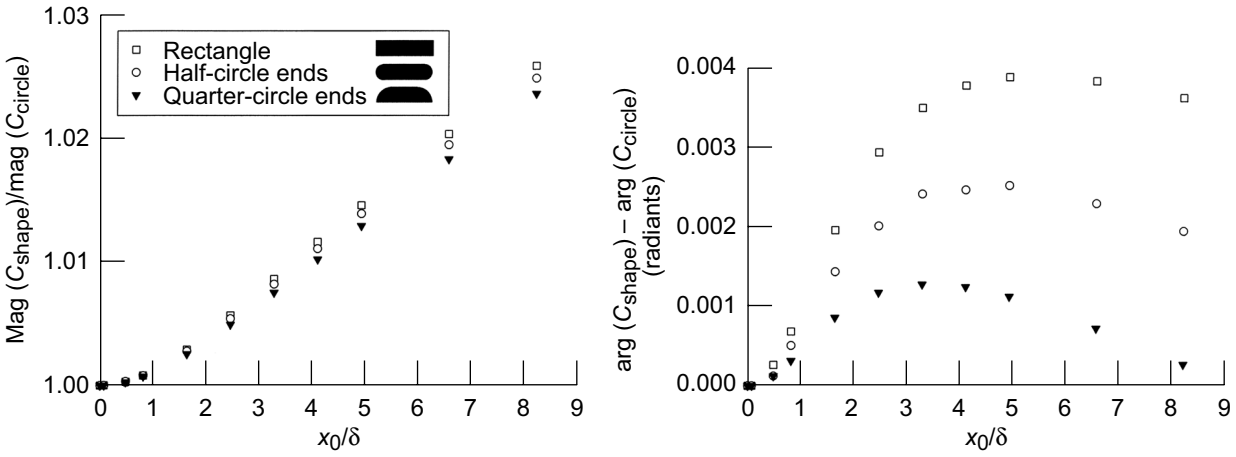

Figure 6.—Numerical calculations at 1 Hz using three alternate cross sections showed that the shape of the cross section had only a small effect on the magnitude and phase of the amplitude function C (x_0/δ, R/δ). The three shapes (shown in the inset) were a rectangle (8×30 μm), a rectangle with half inch ends (30 μm width, 4 μm radii), and a rectangle with quarter-circle ends (30 μm width, 8 μm radii). The results are normalized by those for the circle (13.4 μm radius) that was used in the main numerical calculations. The third shape resembled that of the experimental oscillator, and its results were used as a small correction of the experimental data.

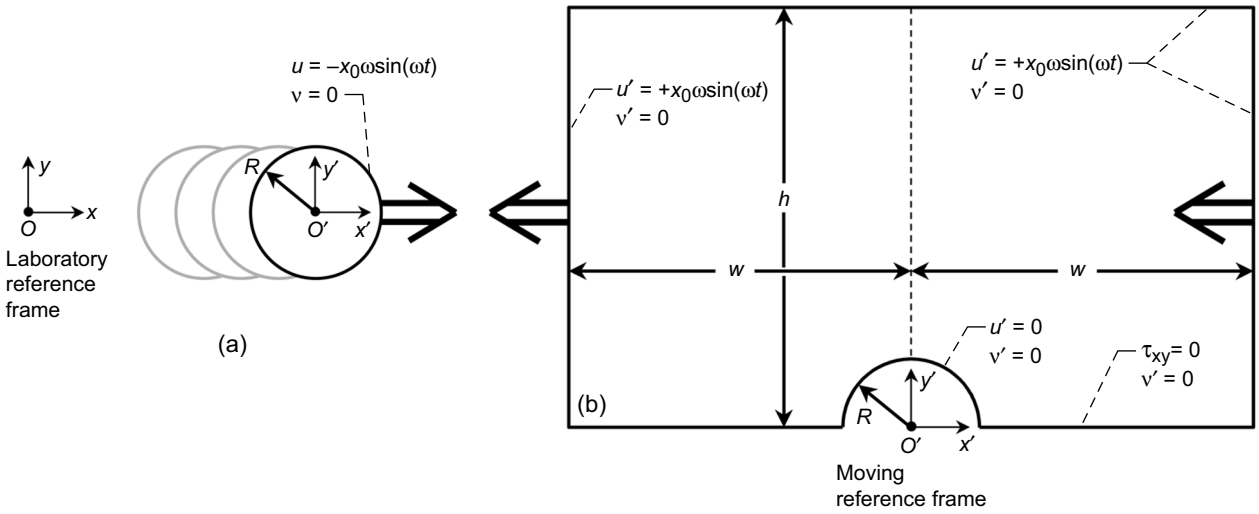

Figure 7.—(a) Schematic illustration of the simplified flow problem of a circular cylinder oscillating in an incompressible incompressible fluid. In the laboratory (inertial) reference frame xOy the velocity of the cylinder is $-x_0\omega\sin(\omega t)$ in the x-direction. In the moving (non-inertial) reference frame $x'O'y'$ attached to the center of the oscillating cylinder the cylinder is motionless. (b) The domain and boundary conditions used in the two-dimensional numerical simulations. Use of the reference frame $x'O'y'$ made the cylinder stationary while the surrounding fluid oscillated sinusoidally in the x-direction. The lengths w and h defined the size of the computational domain. The domain included only $y \geq 0$ due to the assummed symmetry with respect to the x-axis.

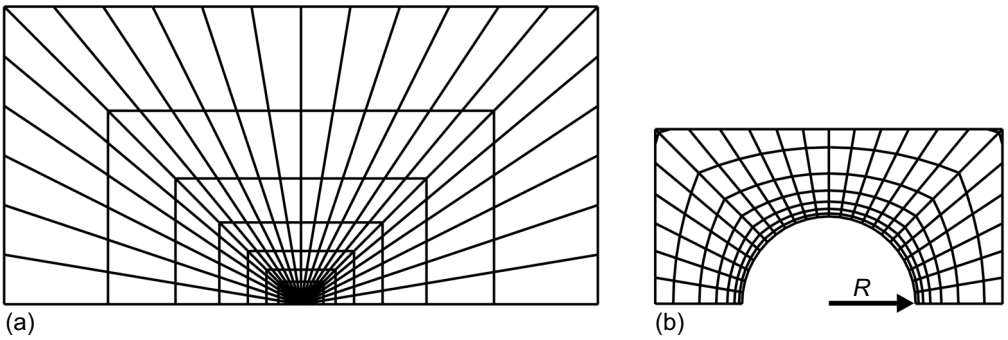

Figure 8.—Finite element mesh used in the validation test with 576 quadrilateral elements and a grading ratio $q = 0.65$. (a) Global view of the mesh bounded by $-2000R < x < 2000R$ and $y < 2000R$; (b) Enlarged view of the mesh grading near the cylinder in a local area bounded by $-2R < x < 2R$ and $y < 2R$.

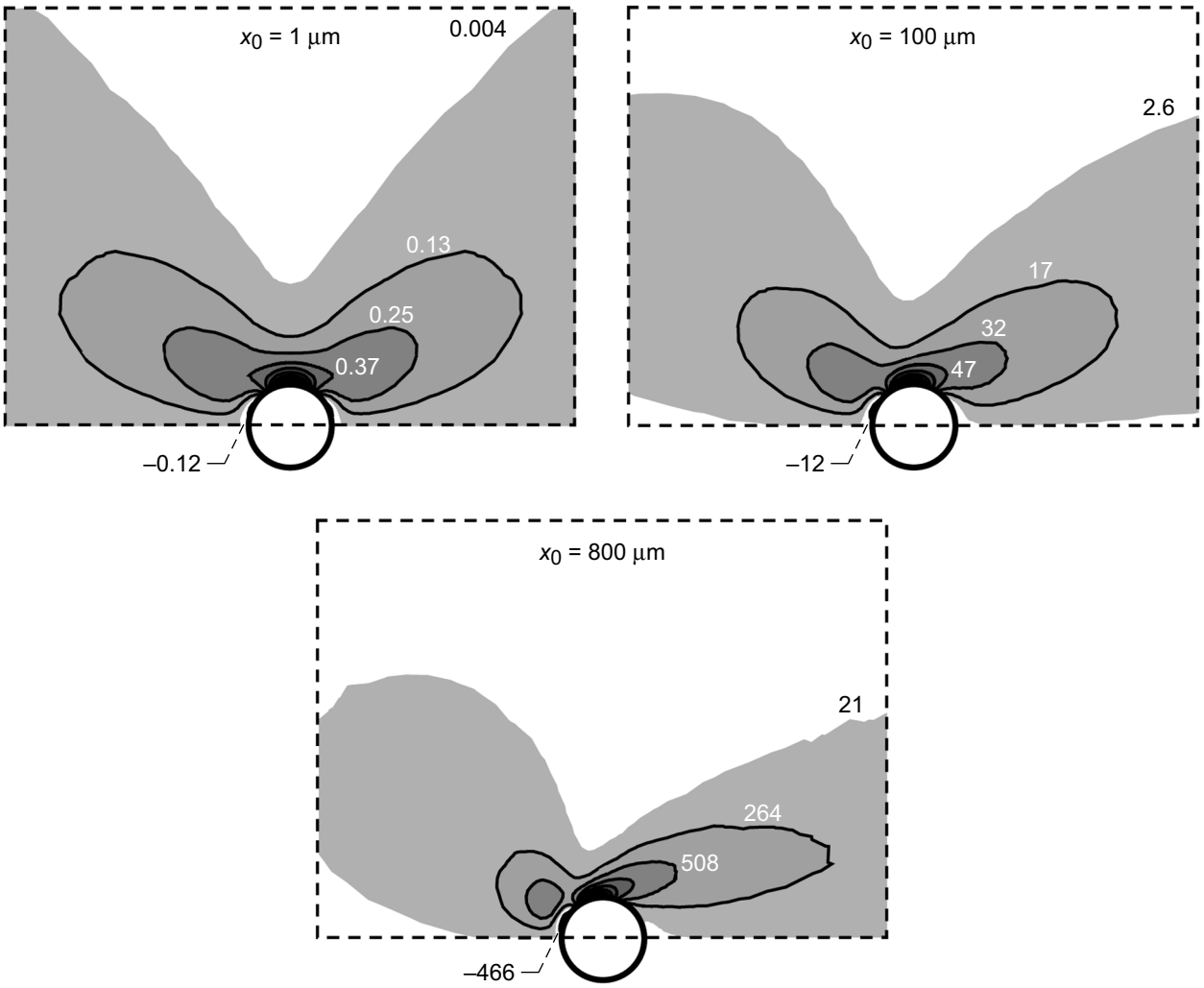

Figure 9.—Selected contours of the shear component of the rate-of-deformation tensor D_{xy} indicated the concentrations of viscous stress near the cylinder at 5 Hz. (Unit's are s^{-1}.) Each map was calculated during the last cycle when cylinder was moving from right to left at maximum speed. Asymmetry is clearly visible at x_0 = 800 μm (x_0/δ = 14.7).

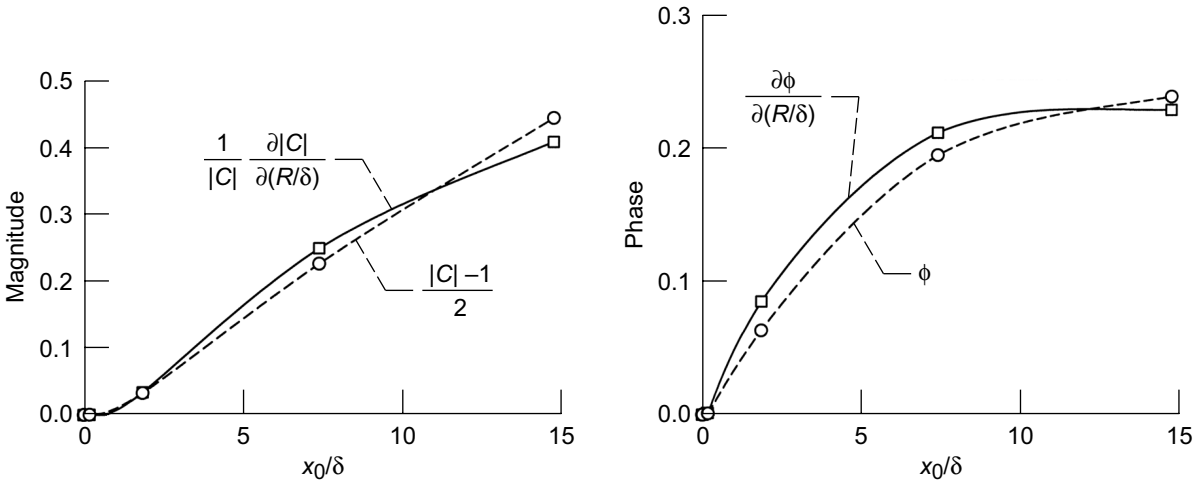

Figure 10.—The derivation of $\partial C/\partial R$ was estimated from the difference C [x_0/δ, (13.4 μm)/δ]–C [x_0/δ, (6.7 μm)/δ]. (left) The normalized derivative of magnitude $|C|$ with respect to R/δ was approximately described by a simple linear function of $|C|$. (right) The derivative of phase ϕ with respect to R/δ was approximately described by ϕ. (The curves are merely guides to the eye).

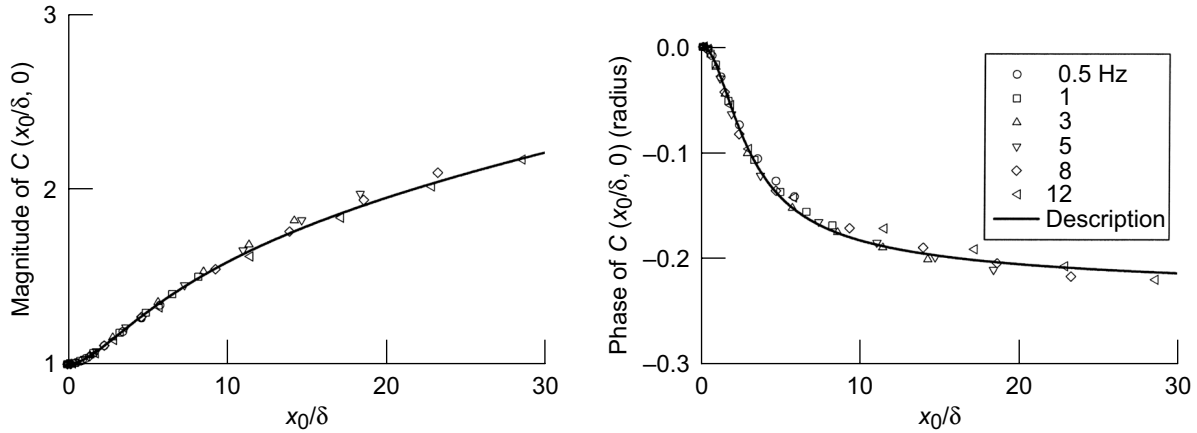

Figure 11.—Numerically calculated magnitude and phase of the amplitude function C (x_0/δ, 0) as a function of reduced amplitude. Eq. (22) was used to adjust the data to $R/\delta = 0$ which is equivalent to an extrapolation to 0 Hz at constant x_0/δ. The curves are empirical description given by Eq. (23).

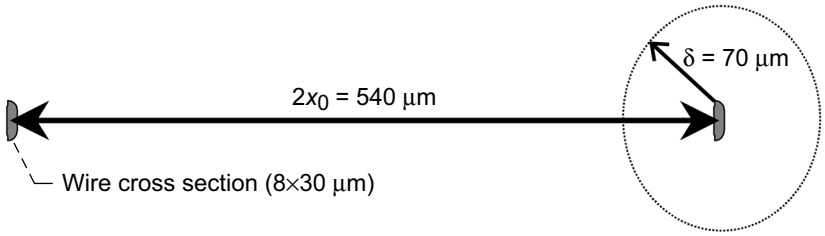

Figure 12.—A single oscillator wire and its maximum displacement x_0 relative to the viscous penetration length δ. The values are for 3 Hz, which gave the largest value of x_0/δ.

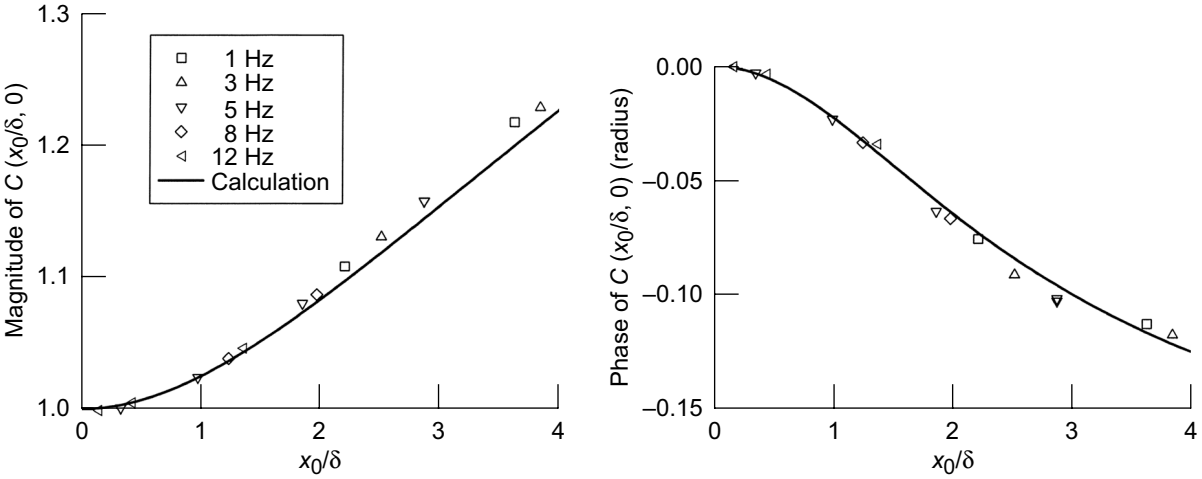

Figure 13.—Measured magnitude and phase of the amplitude function C (x_0/δ, 0) as a function of reduced amplitude. The curves describe the calculated values derived from the data shown in figure 11.

References

[1] J.R. Morison, M.P. O'Brien, J.W. Johnson, and S.A. Schaaf, "The force exerted by surface waves on piles", *J. Petroleum Technology* **2**, 149 (1950).

[2] G.H. Keulegan and Lloyd H. Carpenter, "Forces on cylinders and plates in an oscillating fluid", *J. Res. Nat. Bureau of Standards* **60**, 423 (1957).

[3] P.W. Bearman, M.J. Downie, J.M.R. Graham and E.D. Obasaju, "Forces on cylinders in viscous oscillatory flow at low Keulegan-Carpenter numbers", *J. Fluid Mech.* **154**, 337 (1985).

[4] C.H.K. Williamson, "Sinusoidal flow relative to circular cylinders", *J. Fluid Mech.* **155**, 141 (1985).

[5] T. Sarpkaya, "Force on a circular cylinder in viscous oscillatory flow at low Keulegan-Carpenter numbers", *J. Fluid Mech.* 165, 61 (1986).

[6] P. Justesen, "A numerical study of oscillating flow around a circular cylinder", *J. Fluid Mech.* **222**, 157 (1991).

[7] H. Dütsch, F. Durst, S Becker, and H. Lienhart, "Low-Reynolds-number flow around an oscillating circular cylinder at low Keulegan-Carpenter numbers", *J. Fluid Mech.* **360**, 249 (1998).

[8] B. Uzunoglu, M. Tan, and W.G. Price, "Low-Reynolds-number flow around an oscillating circular cylinder using a cell viscous boundary element method", *Int. J. Num. Methods Eng.* **50**, 2317 (2001).

[9] E. Guilminequ and P. Queutey, "A numerical simulation of vortex shedding from an oscillating circular cylinder", *J. Fluids Struct.* **16**, 773 (2002).

[10] M. Tatsuno and P.W. Bearman, "A visual study of the flow around an oscillating cylinder at low Keulegan-Carpenter numbers and low Stokes numbers", *J. Fluid Mech.* **211**, 157 (1990).

[11] C.L. Morfey and M. Tan, "Unsteady drag on a cylinder due to transverse oscillation at finite amplitude", *J. Sound and Vibration.* **246**, 705 (2001).

[12] R.F. Berg, "Hydrodynamic similarity in an oscillating body viscometer", *Int. J. Thermophys.* **16**, 1257 (1995).

[13] R.F. Berg, M.R. Moldover, and G.A. Zimmerli, "Frequency-dependent viscosity of xenon near the critical point", *Phys. Rev. E* **60**, 4079 (1999).

[14] J.T. Stuart, "Unsteady boundary layers", in *Laminar Boundary Layers*, edited by L. Rosenhead (Oxford University Press, London, 1963). A more accessible reference to $B_{\rm cyl}$ is in R.E. Williams and R.G. Hussey, "Oscillating cylinders and the Stokes paradox", *Phys. Fluids* **11**, 2083 (1972).

[15] R.F. Berg and M.R. Moldover, Science Requirements Document, "CVX-2: Measurement of viscosity dependence on shear rate near the critical point", (1998).

[16] R.F. Berg, M. Yao, M.R. Moldover, and G.A. Zimmerli, "Shear thinning of xenon near the critical point", in preparation (2003).

[17] N. Riley, "Oscillating viscous flows", *Mathematika* **12**, 161 (1965).

[18] J.T. Stuart, "Double boundary layers in oscillatory viscous flow", *J. Fluid Mech.* **24**, 673 (1966).

[19] Certain commercial equipment, instruments, or materials are identified in this paper to foster understanding. Such identification does not imply recommendation or endorsement by the National Institute of Standards and Technology, nor does it imply that the materials or equipment identified are necessarily the best available for the purpose.

[20] Polyflow Version 3.8 User's Manual, Fluent Inc., 10 Cavendish Court, Lebanon, NH 03766 (2000).

[21] A.J. Giacomin and J.M. Dealy, "Using large-amplitude oscillatory shear", in *Rheological Measurements*, 2nd ed., edited by A.A. Collyer and D.W. Clegg, (Kluwer Academic, Dordrecht, 1998).

[22] A.J. Giacomin, R.S. Jeyaseelan, T. Samurkas and J.M. Dealy, "Validity of separable BKZ model for large amplitude oscillatory shear", *J. Rheol.* **37**, 811-826 (1993).

[23] M.J. Reimers and J.M. Dealy, "Sliding plate rheometer study of concentrated polystyrene solutions: Nonlinear viscoelasticity and wall slip of two high molecular weight polymers in tricresyl phosphate", *J. Rheol.* **42**, 527-548 (1998).

[24] M. Wilhelm, D. Maring and H.W. Spiese, "Fourier-transform rheology", *Rheol. Acta.* **37**, 339-405 (1998).

[25] M. Wilhelm, P. Reinheimer and M. Ortseifer, "High sensitivity Fourier-transform rheology", *Rheol. Acta.* **38**, 349-356 (1999).

[26] B. Debbaut and H. Burhin, "Large amplitude oscillatory shear and Fourier-transform rheology for a high-density polyethylene: experiments and numerical simulation", *J. Rheol.* **46**, 1155-1176 (2002).

[27] W.H. Press, S.A. Teukolsky, W.T. Vetterrling and B.P. Flannery, *Numerical Recipes in FORTRAN*, 2nd ed. (Cambridge University Press, New York,1992).

REPORT DOCUMENTATION PAGE	Form Approved OMB No. 0704-0188

1. REPORT DATE *(DD-MM-YYYY)*	2. REPORT TYPE	3. DATES COVERED *(From - To)*
01-12-2007	Final Contractor Report	

4. TITLE AND SUBTITLE
Hydrodynamic Force on a Cylinder Oscillating at Low Frequency

5a. CONTRACT NUMBER
C-32067-J

5b. GRANT NUMBER

5c. PROGRAM ELEMENT NUMBER

6. AUTHOR(S)
Berg, Robert, F.; Yao, Minwu; Panzarella, Charles, H.

5d. PROJECT NUMBER

5e. TASK NUMBER

5f. WORK UNIT NUMBER
WBS 253225.04.01.02.05.03.03

7. PERFORMING ORGANIZATION NAME(S) AND ADDRESS(ES)
National Aeronautics and Space Administration
John H. Glenn Research Center at Lewis Field
Cleveland, Ohio 44135-3191

8. PERFORMING ORGANIZATION REPORT NUMBER
E-16266

9. SPONSORING/MONITORING AGENCY NAME(S) AND ADDRESS(ES)
National Aeronautics and Space Administration
Washington, DC 20546-0001

10. SPONSORING/MONITORS ACRONYM(S)
NASA

11. SPONSORING/MONITORING REPORT NUMBER
NASA/CR-2007-215050

12. DISTRIBUTION/AVAILABILITY STATEMENT
Unclassified-Unlimited
Subject Category: 34
Available electronically at http://gltrs.grc.nasa.gov
This publication is available from the NASA Center for AeroSpace Information, 301-621-0390

13. SUPPLEMENTARY NOTES

14. ABSTRACT

The hydrodynamic force on a cylinder oscillating transversely to its axis is a nonlinear function of the displacement amplitude x_0. We report measurements and numerical calculations of the force at frequencies low enough that $\delta > R$, where δ is the viscous penetration length and R is the cylinder radius. For small amplitudes, the numerically calculated Fourier transform of the force per unit length, $F^{\wedge}_{small}$, agrees with Stokes analytical calculation. For larger amplitudes, the force per unit length found by both calculation and measurement is $F^{\wedge} = F^{\wedge}_{small} C(x_0/\delta, R/\delta)$. The complex function C depends only weakly on R/δ, indicating that x_0/δ is more appropriate as a scaling variable than the Keulegan-Carpenter number $KC = \pi x_0/R$. The measurements used a torsion oscillator driven at frequencies from 1 to 12 Hz while immersed in dense xenon. The oscillator comprised cylinders with an effective radius of R =13.4 μm and oscillation amplitudes as large as $x_0/\delta = 4$ (corresponding to KC as large as 71). The calculations used similar conditions except that the amplitudes were as large as $x_0/\delta = 28$.

15. SUBJECT TERMS
Finite element; Keulegan-Carpenter number; Oscillating cylinder; Stokes viscous parameter; Viscous penetration length; Xenon; Hydrodynamics

16. SECURITY CLASSIFICATION OF:			17. LIMITATION OF ABSTRACT	18. NUMBER OF PAGES	19a. NAME OF RESPONSIBLE PERSON
a. REPORT	b. ABSTRACT	c. THIS PAGE			STI Help Desk (email:help@sti.nasa.gov)
U	U	U	UU	46	19b. TELEPHONE NUMBER *(include area code)* 301-621-0390